Compact, Highly Efficient Huygens Antenna Array with Low Sidelobe and Backlobe Levels

Wei Lin, *Senior Member, IEEE* and Richard W. Ziolkowski, *Life Fellow, IEEE*

***Abstract*—An innovative Huygens antenna array is reported. It has a compact cross section and simultaneously exhibits high aperture and radiation efficiencies and low sidelobe and backlobe levels. The fundamental system consists of a collinear 1×4 magnetic dipole (MD) array unified with an in-phase collinear 1×4 electric dipole (ED) array. The MD array is realized as $TE_{0.5,0}$ – mode SIW waveguide sections with seamlessly integrated phase inverters. The ED array is accomplished with two metal plates orthogonally connected to the waveguide aperture. Low sidelobes are realized thanks to a natural magnitude taper of the fields radiated by each Huygens section located further from the waveguide center where its excitation resides. This fundamental array is easily expanded to a 4×4 array facilitated by an amplitude-weighted 1-to-4 microstrip feed network. An X-band prototype operating at 10 GHz was fabricated and tested. The measured and simulated results are in very good agreement. The measured $|S_{11}|$ bandwidth is 570 MHz from 9.63 to 10.2 GHz. The measured realized gain is stable across the entire bandwidth with a 17.5 dBi peak value. All measured sidelobe and backlobe levels are less than –20 dB. The measured realized aperture efficiency is 67.0% and the simulated radiation efficiency reaches 92%.**

***Index Terms*—Antenna arrays, aperture efficiency, backlobes, complementary sources, Huygens sources, sidelobes.**

I. INTRODUCTION

Sidelobe and backlobe levels are critical performance characteristics of antenna radiation patterns [1]. High sidelobe and backlobe levels represent wasted radiated energy and can lead to unwanted signal interference [2]. They can also increase the noise level in a receiver [3]. For example, radar systems require all sidelobes to be less than –20 dB [4], [5].

Many efforts have been made to suppress the sidelobe levels in antenna arrays as reported in [6]–[28]. However, they face the common challenge that achieving a high aperture efficiency (i.e., larger than 50%) is difficult. Since the main methodology for sidelobe suppression is to taper the amplitudes exciting the array's elements from its central ones to those on its outer edges, there is a corresponding tradeoff between the sidelobe levels and the maximum directivity.

Arrays reported with low sidelobe levels (SLLs) include, for example, microstrip patch arrays [6] – [11] and slot arrays [12] – [17]. Their tapered amplitudes were achieved through their feed networks. However, the aperture efficiencies of these designs are no larger than 50%. For instance, the aperture efficiency of the filtering 1×8 microstrip patch antenna array in [6], the 4 × 4 patch array in [7], the 6 × 6 patch array in [8], the 8×8 slot antenna array in [12], and the 16×16 cavity-backed slot array in [13] are, respectively, 18%, 43%, 0.3%, 32% and ~50%. A second popular approach to achieve the desired amplitude taper is to modify each individual radiating element, e.g., to change its size or shape or loading as in [18] – [28]. Again, their aperture efficiencies are low. For example, the maximum aperture efficiency of the 1×7 [18], 1×10 [19] and 1×12 [20] series-fed microstrip patch antenna arrays, and the 2×6 microstrip patch antenna array loaded with complementary split-ring resonators (CSRRs) in [21] was only 36%.

Recall that the aperture efficiency of an array antenna whose physical area is A is defined as the ratio of its peak directivity to its maximum achievable directivity, D_{max}, where $D_{max} = 4\pi A/\lambda^2$, λ being the wavelength of its source [29]. Note that this definition of the aperture efficiency does not account for any of the antenna's dielectric and conductive losses nor its associated feed network nor the impedance mismatch of the antenna with its source at its input port. To take into consideration of all these losses, the realized aperture efficiency is defined herein as the ratio of the realized gain of the antenna to its maximum achievable directivity, D_{max}. It is specifically introduced to facilitate making fair performance comparisons with the referenced low SLL arrays. The low realized aperture efficiency in all of the noted reported low SLL designs arises from the fact that large portions of their radiating apertures do not contribute effectively to the total radiated power. The main drawback of a low efficiency, of course, is the ineffective utilization of the input power. It remains very challenging to achieve arrays with both low sidelobe levels and high realized aperture efficiency simultaneously.

In this work, we report an innovative Huygens antenna array formed by elements that are pairs of orthogonal and in-phase electric and magnetic dipoles, i.e., Huygens dipole antennas, which individually radiate a cardioid pattern. It has a compact cross-section and achieves high aperture and radiation efficiencies, and low sidelobe and backlobe levels, simultaneously. The fundamental system consists of a collinear 1×4 magnetic dipole (MD) array unified with an in-phase collinear 1×4 electric dipole (ED) array. The MD array is realized as $TE_{0.5,0}$–mode SIW waveguide sections with seamlessly integrated phase inverters. The ED array is accomplished with two metal plates that are orthogonally connected to the sides of the waveguide aperture and extend

Manuscript received Oct. 1, 2020. This work was supported by the UTS Chancellor's Postdoctoral Fellowship under Grant PRO18-6147.

The authors are with the Global Big Data Technologies Centre, School of Electrical and Data Engineering, University of Technology Sydney, Ultimo, NSW 2007, Australia (email: Wei.Lin@uts.edu.au; Richard.Ziolkowski@uts.edu.au)

Color versions of one or more of the figures in this communication are available online at http://ieeexplore.ieee.org.

from it. Being a linear array, high gain Huygens cardioid patterns with a wide beamwidth in the E-plane and narrow beamwidth in the H-plane are obtained. Low sidelobe levels are realized thanks to a natural magnitude taper of the fields radiated by each Huygens section located further from the waveguide center where its excitation resides. This fundamental array is then easily expanded to a 4×4 array facilitated by an amplitude-weighted 1-to-4 microstrip feed network. An X-band prototype operating at 10 GHz was fabricated and tested. The measured results confirmed its exceptional simulated performance. The –10-dB impedance bandwidth is 570 MHz from 9.63 to 10.2 GHz. The realized gain values are stable across the entire bandwidth. The measured (simulated) peak realized gain is 17.5 dBi (18 dBi). All sidelobe and backlobe levels of the measured realized gain patterns are less than -20 dB. The measured (simulated) realized aperture efficiency is 67% (72.7%). The simulated radiation efficiency is 92%.

The remaining sections of this paper are organized as follows. Sec. II introduces the design of the fundarmental 1×4 Huygens antenna array, discusses its perforance characteristics, and explains its operating mechanisms. Sec. III presents the expanded 4×4 Huygens antenna array along with its simulated and measured results. Finally, Sec. IV draws some conclusions and gives a detailed performance comparison between our work and antennna arrays reported with reduced sidelobe levels. All of the numerical simulations and their optimizations reported herein were performed using the commercial software ANSYS Electromagnetics Suite (HFSS), version 19.

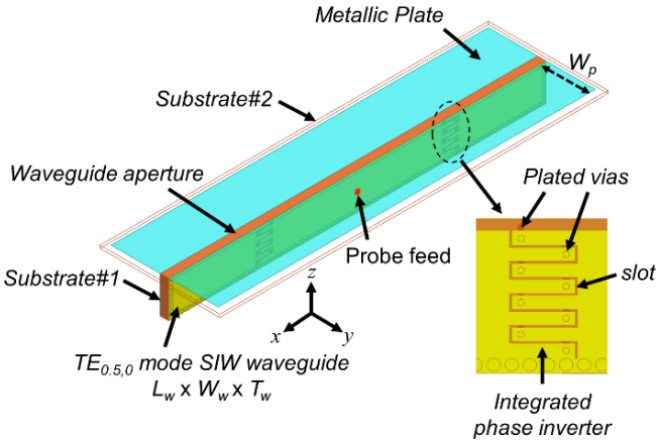

Fig. 1. Configuration and design parameters of the 1×4 Huygens antenna array. The inset depicts one of the two 180º phase inverters that are seamlessly integrated into the waveguide.

II. 1 × 4 Huygens Antenna Array

The configuration of the 1×4 Huygens antenna array is shown in Fig. 1. The design parameters are also indicated. Their optimized values are listed in Table I. The entire antenna array is simple and compact. It consists of two copper-clad Rogers Duroid™ 5880 substrates, each with a 2.2 dielectric constant, a 0.0009 loss tangent, and 0.018 mm thick copper. The $TE_{0.5,0}$–mode SIW waveguide is built with *Substrate#1*, which is 1.575 mm thick. A probe excitation is located in the middle of the waveguide. Two seamlessly integrated 180º phase inverters are located symmetrically with respect to the probe, dividing the waveguide into four sections of equal length. The phase inverter simply consists of eight shorting vias and a meandered slot. The vias are alternatively distributed on two sides of the slot. The detailed design and analysis of this phase inverter can be found in our previously reported work [30]. Two metallic plates are etched on *Substrate#2,* which is 0.787 mm thick. The two plates are orthogonally connected to the waveguide aperture, one on each of its sides and extending from them.

TABLE I:
Parameters of the 1×4 Huygens Antenna Array
(Dimensions in Millimeters)

Parameter	Description	Value
L_w	Length of the waveguide	69
W_w	Width of the waveguide	6.7
T_w	Thickness of the waveguide	1.575
W_p	Width of each of the two metallic plates	9.0
R_p	Radius of the probe	0.5
d_p	Distance of the probe to the aperture	3.5

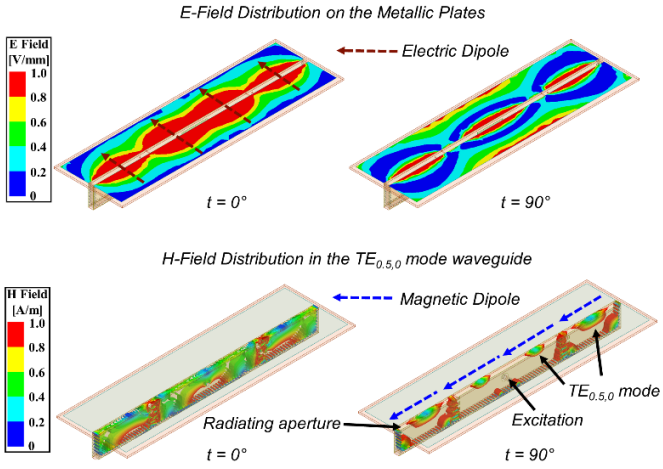

Fig. 2. Electric field distributions on the metallic plates and the magnetic field distributions in the SIW waveguide at quarter periods of time corresponding to its resonance frequency, 10.0 GHz.

A. Operating mechanisms

With only one excitation port, an array of four magnetic dipoles and an array of four electric dipoles are realized in a compact structure. The total electrical length of that aperture is approximately two wavelengths at its resonance frequency. The two 180˚ phase inverters divide the SIW waveguide into four half-wavelength sections such that the electric fields of the four magnetic dipoles along the entire aperture are in-phase and point in the same direction. The four magnetic dipoles represent the equivalent currents associated with those four sections of the open aperture of the SIW waveguide. The four electric dipoles similarly correspond to each half-wavelength section of the metal plates which are attached orthogonal to and extend away from the edges of the open aperture. The MDs and EDs

are orthogonal to each other and radiate in-phase. Their amplitudes are properly balanced and the Huygens cardioid radiation pattern is successfully obtained. The overall radiation pattern of these four collinear Huygens dipole elements is highly directive in the zx-plane, along the length of the waveguide, and has a very broad beamwidth in the orthogonal yz-plane.

Figure 2 shows the magnitudes and directions of the electric fields on the metallic plates and the magnetic fields in the waveguide at two quarter periods of time corresponding to its resonance frequency, 10 GHz. It is clearly seen that the resonant peaks of the electric and magnetic fields alternate between each quarter period, i.e., when the electric fields on the plates are maximum at t = 0˚, the magnetic fields in the waveguide are minimum. The opposite is found at t = 90˚. Note that the equivalent magnetic currents on the waveguide aperture, i.e., $\vec{K}_s = -\hat{n}_s \times \vec{E}_{tan}$, where $\hat{n}_s$ is the unit vector normal to the aperture and $\vec{E}_{tan}$ is the tangential component of the electric field in the aperture [31], have a 90˚ phase difference ahead of the electric currents $\vec{J}_s$ on the walls of the waveguide associated with the magnetic fields in it. Consequently, the electric and magnetic current moments are in-phase, as required by the balanced condition of a Huygens source [32].

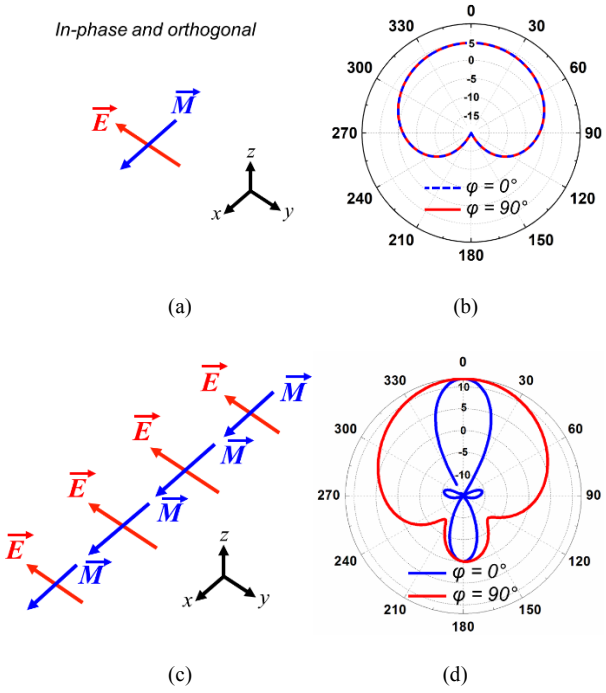

Fig. 3. Four element Huygens dipole antenna array. (a) Ideal single Huygens dipole element. (b) Cardioid directivity patterns in the two principal vertical planes. (c) Equivalent electric and magnetic dipoles corresponding to each quarter-wavelength section of the waveguide. (d) Realized gain (dBi) patterns in the two principal vertical planes at the resonance frequency, 10 GHz.

Fig. 3 (a) shows the idealized Huygens dipole element, i.e., one pair of orthogonally-orientated and in-phase electric ($\vec{E}$) and magnetic ($\vec{M}$) dipoles. The Huygens cardioid pattern that it radiates is shown in Fig. 3 (b). Fig. 3(c) illustrates the $\vec{E}$ and $\vec{M}$ dipole elements that constitute the array and that are associated with each quarter-wavelength section of the waveguide. The four pairs of orthogonally oriented and in-phase ED and MD radiators form the four Huygens dipole elements of the array. Thus, the entire antenna is a 1 × 4 Huygens array. Fig. 3(d) shows the simulated realized gain patterns of the four-element Huygens array in its two principal vertical planes. They have their maximum in the broadside direction. The E-plane (φ = 90°) pattern, orthogonal to the length of the array, has a wide beamwidth and the associated H-plane (φ = 0°) pattern, along the length of the array, has a narrow beamwidth. This radiation pattern is exceptional for wireless applications that require both broad coverage and high directivity. The peak gain in the broadside direction is 11.8 dBi and the 3-dB beamwidth in the E-plane is 90°. The realized aperture efficiency is 72%. Moreover, the sidelobe level in the H-plane is less than –20 dB thanks to the naturally tapered E- and H-fields distributions that result as the quarter-wavelength sections move further away from the source. It is clearly seen in Fig. 2 that both the E-fields and H-fields in the middle two sections are stronger than those in the outer two sections.

These patterns have the forms expected from previously reported Huygens sources relying on similar electromagnetic behaviors. The many magnetoelectric (ME) dipole antennas developed by Prof. Luk and his co-authors and others, e.g., in [33]–[38], which refer to the Huygens dipole pairs as complementary sources, display many of the same properties. Our previously reported Huygens dipole antennas in [39]–[41], which in contrast are electrically small, do as well. Nevertheless, the backlobe is higher than desired yielding only a modest –12 dB front-to-back ratio (FTBR).

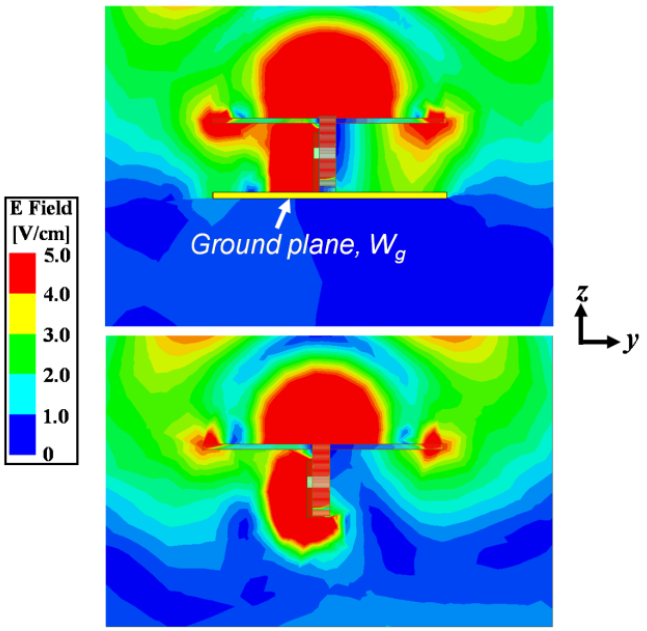

Fig. 4. Magnitude of the electric fields near the array in the *yz*-plane at 10 GHz. (Upper) With a compact metallic ground plane. (Below) Without the ground plane.

B. Further critical design considerations

The backlobe level in Fig. 3(b) is a bit high mainly because of the diffracted fields from both edges of the plates [42]. This effect is seen in the E-field distributions near the array in the bottom subplot of Fig. 4. To effectively mitigate this back radiation, a compact metallic ground is attached to the bottom of the waveguide and, hence, is beneath the two plates. The size of this ground plane is the same as the radiating aperture and the distance from the two ED plates is equal to the width of the waveguide. It is clearly seen from the E-field distributions shown in the upper subplot of Fig. 4(b) that introducing this compact ground plane effectively mitigates the back radiation.

A comparison of the simulated gain patterns of the array with and without the ground plane at 10 GHz is given in Fig. 5(a). It confirms the backlobe level improvement when the ground plane is present. The front-to-back ratio (FTBR) improves 6.5 dB to 18.5 dB. Fig. 5(b) shows the 3D radiation pattern at 10 GHz with the ground plane being present. It has several exceptional features: high directivity and wide beamwidth in the E-plane, as well as low sidelobe and backlobe levels. The peak broadside gain and realized aperture efficiency have also improved to 12.0 dBi and 75%, respectively. This type of gain pattern is highly coveted in applications requiring large coverage, long distance operation, and reduced signal interference simultaneously.

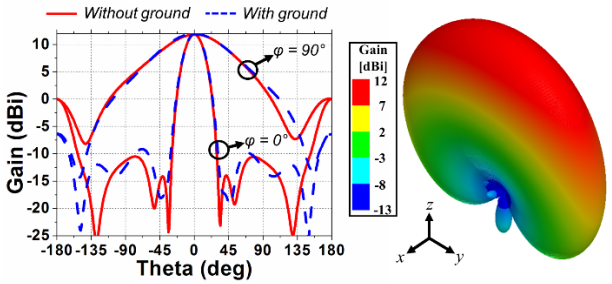

(a) (b)

Fig. 5. Effect of adding a ground plane beneath the radiating plates. (a) Demonstration of the backlobe level improvement from the radiation patterns at 10 GHz. (b) 3D radiation pattern at 10 GHz with ground plane.

The width of the ground plane was not randomly chosen. Fig. 6(a) shows the radiation patterns when the width of the ground, W_g, varies from 10 mm to 30 mm in 10 mm intervals. It is observed that the FTBR reaches its maximum value, 18.5 dB, only if W_g = 20.0 mm, i.e. if the width of the ground plane is very close to the total width of the top radiating aperture, 19.58 mm. The FTBR values for both smaller ground (W_g = 10 mm) and larger ground (W_g = 30 mm) are only 15.0 dB. The reason that the backlobe is suppressed when the ground plane and the entire top radiating electric aperture are the same size can be described from a transmission line point of view. Consider the plates and the ground plane as a parallel-plate transmission line. The back radiation mitigation happens because there is now an open circuit across the long outside edges. The waves traveling to the outside long edge of the ED plates are reflected back away from them and, hence, the diffracted fields are decreased significantly. Consequently, the ground width, W_g = 20 mm, was chosen for the final design.

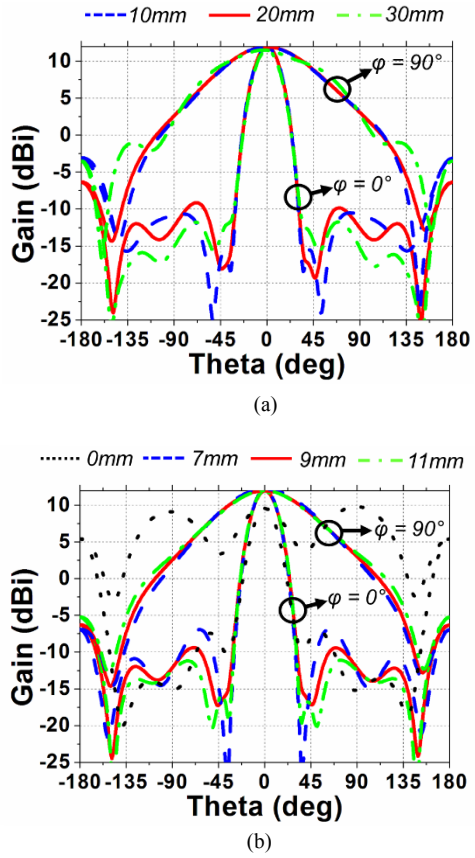

Fig. 6. Parametric studies. (a) Comparison of radiation patterns at 10 GHz when the width of the ground, W_g, varies from 10.0 to 30.0 mm. (b) Comparison of radiation patterns at 10 GHz when the width of the radiating plates, W_p, varies from 0 to 11.0 mm.

Another key design parameter is the width of each of the two radiating plates, W_p. Fig. 6(b) compares the radiation patterns of the antenna with the presence of the ground plane (with W_g = 20.0 mm) as W_p varies from 0.0 to 11.0 mm. One immediately finds that the presence of the two plates is critical to produce the unidirectional Huygens pattern. The pattern deteriorates significantly if no plate is present (W_p = 0 mm). Although the broadside gain values for the plate width between 7.0 and 11.0 mm are similar, ~ 12.0 dBi, their sidelobe levels are different. To obtain the lowest sidelobe level, the plate width, W_p = 9.0 mm, was chosen for the final design.

Since the entire antenna configuration is compact and simple, its design guidelines for an arbitrary operating frequency are quite straightforward. First, the electrical length of the SIW waveguide is set to be two free-space wavelengths (λ_0) for a 4-element array. Two integrated 180º phase inverters [30] are placed symmetrically with respect to the center of the waveguide. Once the design of the MD elements is completed, the two metallic plates are incorporated into it. These plates are oriented orthogonal to the large sidewalls of the waveguide and connected to its top edges. A ground plane with the same size as

the overall top radiating aperture that now includes the plates is placed underneath and connected to the bottom of the waveguide. Its length is the same as the waveguide and the initial value for its width and the total width of both plates plus the waveguide aperture's gap can be set as 0.6 λ_0. The final design is then obtained with a few simulations to optimize the various dimensions of the system.

Note that this 4-element array could have been easily extended to more elements by increasing the lengths of the waveguide and the metal plates in both directions to achieve higher peak gains. One simply would need to introduce an additional phase inverter at every half wavelength position. This strategy was considered successfully for the related omnidirectional magnetic dipole (OMD) array in [28]. The 1×4 array developed herein was a simple choice for the proof-of-concept demonstration.

III. Expanded 4 × 4 Huygens Antenna Array

While the single excitation port of the 1×4 Huygens array is convenient for many applications, many others require yet higher maximum gain values. The fundamental design can be easily expanded to a larger scale, e.g., a 4×4 array with a higher broadside peak gain value, but with similar low sidelobe and backlobe levels. This expanded version is facilitated by a introducing a linear 1-to-4 feed network that distributes a specified tapered amplitude distribution to the array elements.

A. System Configuration

The disassembled configuration of the expanded 4×4 Huygens antenna array is shown in Fig. 7. The entire array consists of three main sections that include four pairs of radiating plates (EDs), four $TE_{0.5,0}$–mode SIW waveguides (MDs) with two integrated 180º phase inverters in each of them, and with microstrip line to probe transitions also integrated into them that are excited with a 1-to-4 microstrip feed network.

The array is constructed entirely from four pieces of the Rogers Duroid™ 5880 substrate. Consider the isometric view in Fig. 7(a) from the top to the bottom. There are four pairs of metallic plates etched on upper surface of the PCB, *Sub#1,* whose thickness is 0.508 mm. The center-to-center distance between the adjacent pairs is D_{array}. There are four identical SIW waveguide systems, each one located immediately beneath a pair of these plates. Each is built on one PCB, *Subs#2*, whose thickness is 1.575 mm. The plates are orthogonal to the edges of the waveguide apertures and each pair is connected to one of them as they were in the fundamental 1×4 Huygens array. The 1-to-4 microstrip feed network is implemented on the bottom PCB, *Sub#4*, whose thickness is 0.508 mm. However, unlike the base 1×4 array design, there is another set of four small rectangular PCBs, the *Subs#3* pieces, whose thicknesses are 0.508 mm. Each one is attached to a single waveguide. The waveguide wall acts as a ground plane for the copper trace on the outside surface of each one.

The vertical 50–Ω microstrip lines on the *Subs#3* elements function as the transition elements from the 50–Ω microstrip line of the feed network to the probe excitation element of that waveguide section. Note that the locations of the excitation probes are closer to the waveguide aperture. They are connected to both the outputs of the feed network on *Sub#4* and to the excitation probes in the waveguides. The impedance matching is realized by two sets of impedance transformers as shown in Fig. 7(a). The first set, denoted as impedance transformer #1, connects the four outputs of the feed network to the 50–Ω microstrip line of the probe excitation. Its dimensions are marked as L_{t1} and W_{t1}. The second set, denoted as impedance transformer #2, connects the 50–Ω microstrip line of the feed network to the SMA connector. Its dimensions are marked as L_{t2} and W_{t2}. The dimensions of both sets were optimized numerically. The entire array is fed by a SMA behind the ground plane. The detailed parameters are listed in Table II.

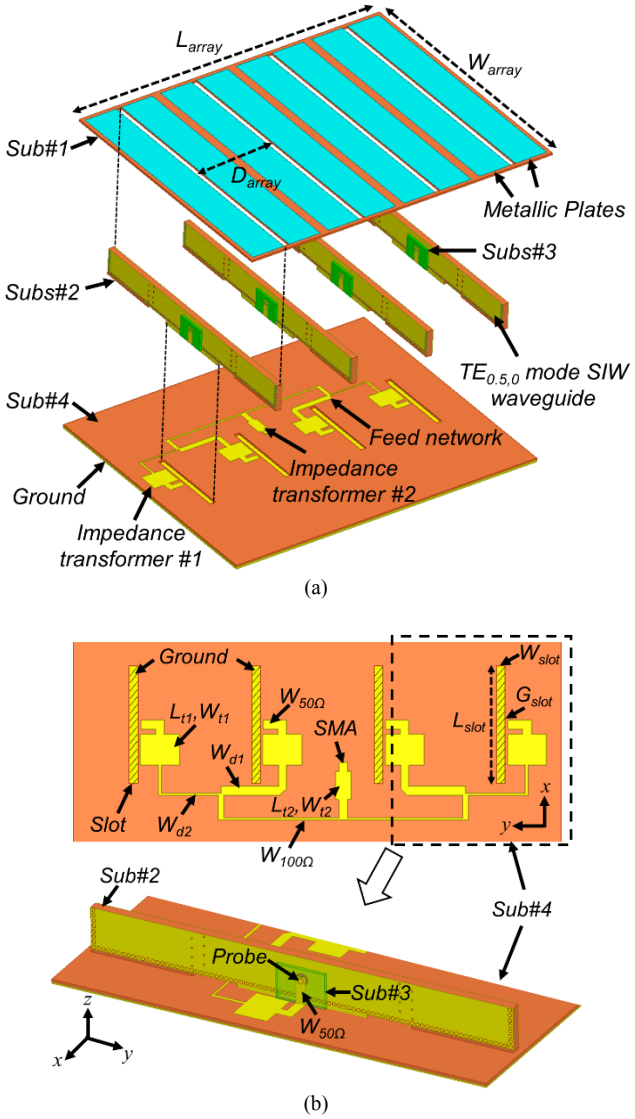

Fig. 7. Expanded view the 4x4 Huygens antenna array configuration. (a) Disassembled view of the three main sections of the array. (b) Detailed view of the feed network and one of the SIW waveguides connected to it.

The amplitudes of the outputs of the feed network that excite each of the 1×4 Huygens arrays are weighted as (0.4, 1, 1, 0.4). The ground plane of the feed network, the bottom copper

surface of *Sub#4,* also acts as the ground plane for all four of the 1×4 Huygens arrays again for improvement of the overall FTBR value. Its size matches that of the top section, $L_{array} \times W_{array}$. All three sections and the U-shaped elements are connected during assembly of the array to form a compact structure.

TABLE II:
EXPANDED 4 × 4 HUYGENS ANTENNA ARRAY PARAMETERS
(DIMENSIONS IN MILLIMETERS)

Parameter	Description	Value
L_{array}	Length of the array	87.58
W_{array}	Width of the array	71.0
D_{array}	Distance between adjacent elements	22.0
H_{array}	Height of the array	7.5
W_{d1}	Width of power divider line#1	1.6
W_{d2}	Width of power divider line#2	0.3
L_{t1}	Length of impedance transformer#1	5.5
W_{t1}	Width of impedance transformer#1	7.0
L_{t2}	Length of impedance transformer#2	5.0
W_{t2}	Width of impedance transformer#2	2.8
L_{slot}	Length of the slots cut on Sub#4	21.2
W_{slot}	Width of the slots cut on Sub#4	1.575
G_{slot}	Gap between the slot and feed network	0.508

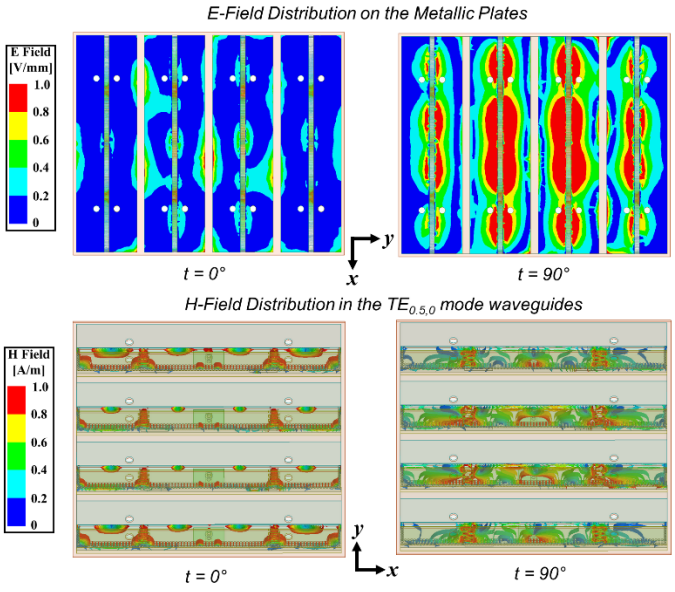

Fig. 8. Electric field distributions on the metallic plates and magnetic field distributions in the SIW waveguides at two successive quarter-periods of time corresponding to the resonance frequency, 10GHz.

B. *Simulated performance characteristics*

The expanded 4×4 Huygens antenna array was simulated to understand and to optimize its performance. The simulations indicate that it simultaneously achieves high directivity, high realized aperture efficiency, and low sidelobe and backlobe levels. The magnitude of electric and magnetic field distributions on the array as shown in Fig. 8. They well explain how its exceptional performance characteristics are attained. It is clearly observed that there are 16 EDs and 16 MDs excited on its effective aperture, i.e., respectively on the plates and on the waveguide aperture. The EDs and MDs are seen to resonate alternately every quarter-period of the resonance frequency. The resulting in-phase set of radiating elements produce a highly directive, unidirectional beam. Low SLLs in all directions are achieved because the magnitudes of the excitations of the EDs and MDs are tapered from the center of the overall array to its edges along both the *x* and *y* directions.

The simulated realized gain patterns shown in Fig. 9 confirm the excellent broadside beam performance of the 4×4 Huygens array. Fig. 9(a) compares the co-polarized (co-pol) and cross-polarized (x-pol) values in the two principal vertical planes at 10 GHz. The peak broadside realized gain reaches 18 dBi and all of the first sidelobe levels in both the E- and H-planes are below –20 dB from it. The backlobe level is less than –30 dB from the peak value giving a FTBR greater than 30 dB. The 3D realized gain pattern in Fig. 9(b) at 10 GHz further demonstrates that all sidelobe and backlobe levels are extremely low over the entire space. Its realized aperture efficiency at the resonance frequency reaches 72.7%, which is the highest among the reported antenna arrays with low SLLs [6]–[28]. The benefit of the Huygens elements is further demonstrated by comparing the 3D pattern of the array with the two metallic plates (i.e., the electric dipoles), Fig. 9(b), and without them, Fig. 9(c). As shown in Fig. 9(c), the pattern deteriorates significantly without the plates. The sidelobe and backlobe levels increase noticeably. Moreover, the peak gain drops around 3dB.

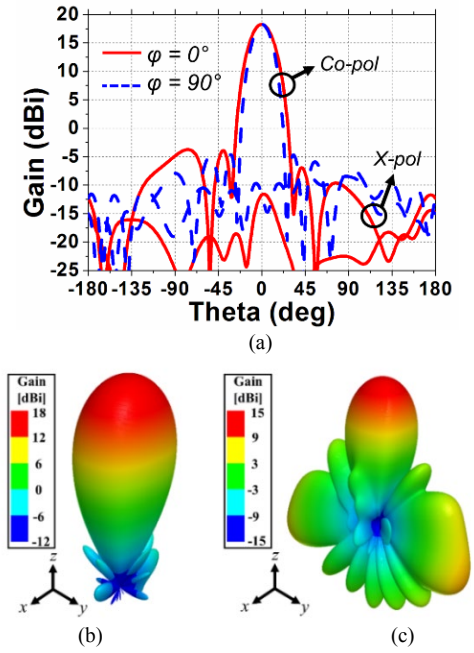

Fig. 9. Simulated realized gain values of the 4 x 4 Huygens array at 10 GHz. (a) 2D realized gain co-pol and x-pol patterns in the two principal vertical planes. (b) Corresponding 3D realized gain pattern. (c) 3D realized gain pattern of the array without the plates to further demonstrate the effectiveness of their presence in the array design.

C. *Fabricated prototype and measured results*

All of the components of the 4×4 Huygens antenna array were fabricated with standard low cost PCB manufacturing

technology. The components were then assembled to form the compact prototype, as shown in Fig. 10. Several plastic strews (4 per 1×4 sub-array) having a 2.0 mm diameter and an aluminum base whose thickness was 1.0 mm were used to enhance the mechanical strength of the antenna structure. The female SMA connector shown in Fig. 10(b) was adopted as the input port. The reflection coefficient, $|S_{11}|$, was measured with a vector network analyzer (VNA) from Keysight Technologies™. The realized gain patterns were measured in a compact range anechoic chamber from MVG Group™.

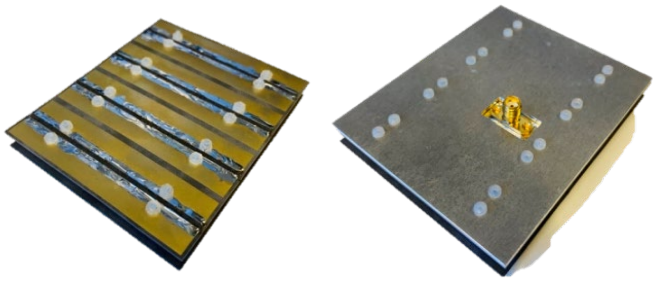

(a) (b)

Fig. 10. Photos of the fabricated 4×4 Huygens antenna array prototype. (a) Front view. (b) Back view

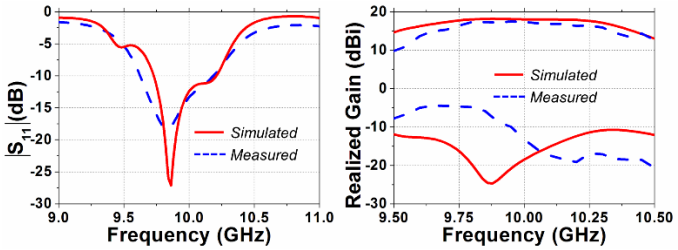

(a) (b)

Fig. 11. Measured and simulated performance characteristics as functions of the source frequency. (a) $|S_{11}|$ values. (b) Realized gain values.

The measured and simulated $|S_{11}|$ and realized gain values as functions of the source frequency are presented in Fig. 11. It is observed that the measured values agree reasonably well with their simulated ones. The measured (simulated) –10-dB impedance bandwidth covers 570 MHz (400 MHz) from 9.63 to 10.2 GHz (9.8 to 10.2 GHz). The co-polarization realized gain values are stable across the entire bandwidth with the maximum variations being within a 3 dB range. The measured cross-polarization level is less than –20 dB. The measured peak realized gain is 17.5 dBi, which is only 0.5 dB lower than its simulated value, 18.0 dBi. This difference is quite reasonable; its decrease also explains the increased bandwidth. Typical system and fabrication tolerances, measurement alignments, and SMA connector losses are responsible for it. The measured (simulated) realized aperture efficiency is 67.0% (72.7%) at 10 GHz. The simulated radiation efficiency is 92%. Note the radiation efficiency is defined as the ratio of the total radiated power to the accepted power from the input port of the antenna array. It is a different figure of merit from the realized aperture efficiency. Radiation efficiency does not include the loss from the impedance mismatch, but the realized gain does. Thus, it is totally reasonable that these two efficiencies have a noticeable difference. Recall that the peak realized gain of an array includes both the concepts of radiation efficiency and aperture efficiency in relation to the maximum possible directivity for a given aperture size and the power at the input port of the system [43]. All of the losses from the feed network, the materials associated with its radiating elements, and the impedance mismatch have been included in these simulated Huygens array results. As noted, the same is true of the measured realized gain results. Thus, the close agreement of the various simulated and measured results indicates that the radiation efficiency of the prototype approaches its simulated value.

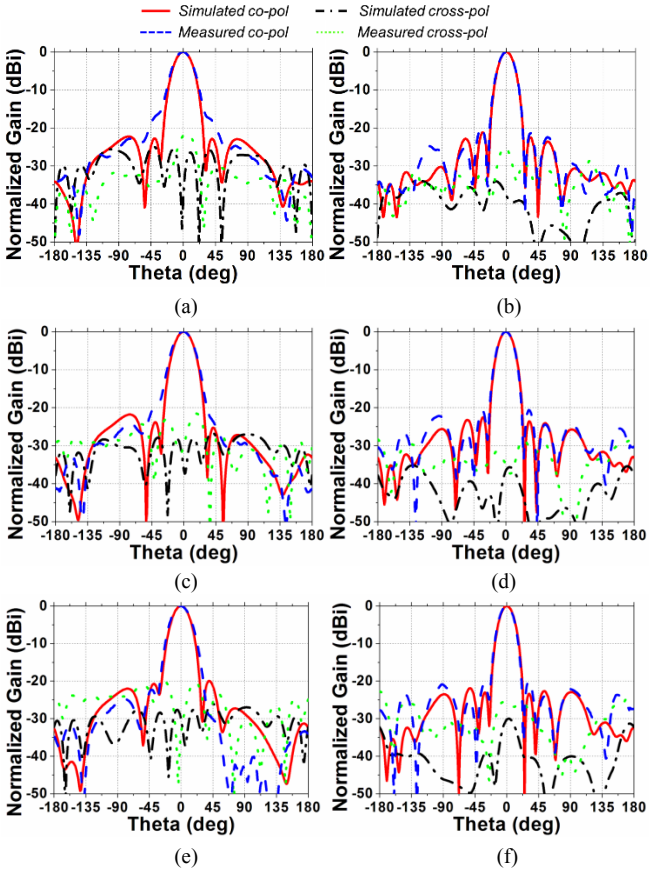

Fig. 12. Measured and simulated normalized realized gain patterns in the two principal vertical planes at different frequencies. (a) 9.8 GHz and $\varphi = 0°$. (b) 9.8 GHz and $\varphi = 90°$. (c) 10 GHz and $\varphi = 0°$. (d) 10 GHz and $\varphi = 90°$. (e) 10.2 GHz and $\varphi = 0°$. (f) 10.2 GHz and $\varphi = 90°$.

Figure 12 compares the measured and simulated normalized realized gain patterns in the two principal vertical E- ($\varphi = 90°$) and H-planes ($\varphi = 0°$) at 9.8, 10.0 and 10.2 GHz. The measured results agree reasonably well with the simulated values. All of the sidelobe and backlobe levels are below –20 dB from the peak value. The cross polarization levels are less than –20 dB from it. The measured and simulated 3-dB beamwidths agree very well at all frequencies. It should be noted that there is a bit of discrepancy between the measured and simulated patterns in the H-plane ($\varphi = 0°$). As checked with simulations, this is due to fabrication tolerances in the realization of the SIW waveguide

TABLE III:
PERFORMANCE COMPARISONS OF THE 4×4 HUYGENS ARRAY PROTOTYPE AND TYPICAL EXAMPLES OF PREVIOUSLY REPORTED ANTENNA ARRAYS

*(): Simulated result

Ref.	Scale	Design Category	BW %	Max SLL Level, FTBR and Peak Realized Gain (dB) (dB) (dBi)			Realized Aperture Eff. %	Radiation Eff. %
[6]	1 × 8	Microstrip patch array	2.86	-19.7	25.0	10.6	~18.0	55.0
[7]	4 × 4	Microstrip patch array	2.1	-26.5	30	18.2	43.0	N/A
[8]	6 × 6	Microstrip patch array	6.4	-20.4	27.0	18.3	0.3	N/A
[12]	8 × 8	Slot antenna array	16	-18.0	30.0	24.0	30.2	41.7
[13]	16 × 16	Slot antenna array	13.8	-25.0	N/A	29.5	~50.0	85.0
[18]	1 × 7	Series-fed patch array	1.4	-28.0	25.0	12.8	~32.0	N/A
[19]	1 × 10	Series-fed patch array	~1	-25.3	N/A	14.5	~25.0	47.0
[20]	1 × 12	Series-fed patch array	6.2	-24.0	N/A	16.0	0.2	96.0
[21]	2 × 6	Loaded patch array	1.8	-23.0	12.6	16.1	36.0	N/A
[36]	1 × 8	ME dipole array	16.4	-10.0	N/A	12.0	< 50	~ 50.0
[37]	4 × 4	ME dipole array	16.4	-10.0	N/A	14.7	< 26	~37.5
[38]	4 × 4	ME dipole array	16.7	-10.0	N/A	19.3	~12	N/A
This Work	**4 × 4**	**Huygens Array (ME dipole array)**	**5.7**	**-20.6 (-20)**	**23 (32)**	**17.5 (18.0)**	**67.0 (72.7)**	**(92.0)**

with its integrated phase inverters, which involves many vias. Small discrepancies in the diameters of the vias accumulate and affect the array pattern in the H-plane where the four magnetic dipoles are aligned. Note in contrast that the measured and simulated patterns in the E-plane ($\varphi = 0°$) agree very well. This outcome is caused by the array pattern in the E-plane being determined by the magnitude and phase of the outputs in the feed network. In contrast to the via diameter errors, the fabrication discrepancies in the microstrip feed networks are minor.

Table III compares the antenna performance characteristics of the 4×4 Huygens array prototype and several examples of antenna arrays reported to have low SLLs. Emphasized features include the array scale; bandwidth; maximum sidelobe level, peak realized gain and FTBR values; and realized aperture and radiation efficiencies. Even though their SLL performance is far from the other comparison examples, which have close to or better than –20 dB maximum SLL values, the ME dipole arrays [36]–[38] are included because their unit elements rely on fundamentally the same radiation physics. Those arrays achieve the highest bandwidths at a cost of their other performance characteristics. It is clearly seen that our design achieves the highest realized aperture efficiency. Its peak realized gain and radiation efficiency values are amongst the best ones. It is compact, simple to realize with standard PCB manufacturing technology and, hence, is low in cost. The scale of the array could be further expanded simply by including more elements and adopting a larger feed network.

IV. CONCLUSION

A new Huygens antenna array design that achieves both high efficiency and low sidelobe and backlobe levels was successfully developed. The fundamental 1× 4 Huygens array was first designed and the parameter studies leading to its optimization were discussed. It was excited by a single coaxial probe. Its simulated radiation performance characteristics were presented. The realized gain patterns were shown to be attractive and suitable for both long distance and broad area coverage, i.e., they exhibited wide beamwidths in the E-plane and narrow beamwidths in the H-plane with high directivity in the broadside direction. A compact 4×4 Huygens array was then realized by combining four of the fundamental 1×4 arrays together. Each of these 1×4 arrays was excited by incorporating a simple 1-to-4 microstrip feed network that delivered weighted excitation amplitudes to them to taper the overall aperture distribution in both directions. Measurements of its fabricated prototype confirmed its exceptional unidirectional main beam and sidelobe and backlobe performance characteristics. It is an ideal candidate for wireless and remote sensing applications that require all sidelobe and backlobe levels to be much lower than its peak broadside gain value.

V. ACKNOWLEDGEMENTS

The authors would like to thank Dr. G. L. Huang, Shenzhen University, for his assistance in the fabrication of the antennas; and Prof. Y. Jay Guo, University of Technology Sydney, for his support of these efforts.

REFERENCES

[1] Z. Hu, W. Wang, Z. Shen and W. Wu, "Low-profile helical quasi-Yagi antenna array with multibeams at the endfire direction", IEEE Antennas Wireless Propag. Lett., vol. 16, pp. 1241–1244, 2017.

[2] D. M. Pozar and B. Kaufman, "Design considerations for low sidelobe microstrip arrays," *IEEE Trans. Antennas Propag.*, vol. 38, no. 8, pp. 1176–1185, Aug. 1990.

[3] J. Teniente, R. Gonzalo, and C. D. Rio, "Low sidelobe corrugated horn antennas for radio telescopes to maximize G/T_s," *IEEE Trans. Antennas Propag.*, vol. 59, no. 6, pp. 1886–1893, June 2011.

[4] R. Bayderkhani and H. R. Hassani, "Wideband and low sidelobe slot antenna fed by series-fed printed array," *IEEE Trans. Antennas Propag.*, vol. 58, no. 12, pp. 3898–3904, Dec. 2010.

[5] J. N. Sahalos, "Design of shared aperture radar arrays with low sidelobe level of the two-way array factor," *IEEE Trans. Antennas Propag.*, vol. 68, no. 7, pp. 5415–5420, July 2020.

[6] F. C. Chen, H. T. Hu, R. S. Li, Q. X. Chu, and M. J. Lancaster, "Design of filtering microstrip antenna array with reduced sidelobe level," *IEEE Trans. Antennas Propag.*, vol. 65, no. 2, pp. 903–908, Feb. 2017.

[7] H. Wang, K. E. Kedze, and I. Park, "Microstrip patch array antenna using a parallel and series combination feed network," in *Proc. 2018 Int. Symp. Antenna Propag. (ISAP2018)*, Busan, Korea, 23-26 Oct. 2018.

[8] K. Xing , B. Liu, Z. Guo, X. Wei, R. Zhao, and Y. Ma, "Backlobe and sidelobe suppression of a Q-band patch antenna array by using substrate integrated coaxial line feeding technique," *IEEE Antennas Wireless Propag. Lett.*, vol 16, pp. 3043–3046, 2017.

[9] L. Wen et al., "A balanced feed filtering antenna with novel coupling structure for low-sidelobe radar applications," *IEEE Access*, vol. 6, pp. 77169–77178, 2018.

[10] T. Li and Z. N. Chen, "Wideband sidelobe-level reduced Ka-band metasurface antenna array fed by substrate-integrated gap waveguide using characteristic mode analysis," *IEEE Trans. Antennas Propag.*, vol. 68, no. 3, pp. 1356–1365, Mar. 2020.

[11] E. Noh, Y. Kang and K. Kim, "Slit-loaded series feed network for millimeter-wave array antenna with a low sidelobe level over a wide bandwidth," *IEEE Trans. Antennas Propag.*, vol. 68, no. 6, pp. 4658–4667, Jun. 2020.

[12] X. Jiang et al., "Ka-band 8 × 8 low-sidelobe slot antenna array using a 1-to-64 high-efficiency network designed by new printed RGW technology," *IEEE Antennas Wireless Propag. Lett.*, vol. 18, no. 6, pp. 1248–1252, Jun. 2019.

[13] G. L. Huang, S. G. Zhou, T. H. Chio, H. T. Hui, and T. S. Yeo "A low profile and low sidelobe wideband slot antenna array fed by an amplitude-tapering waveguide feed-network," *IEEE Trans. Antennas Propag.*, vol. 63, no. 1, pp. 419–423, Jan. 2015.

[14] H. Yang et al., "Improved design of low sidelobe substrate integrated waveguide longitudinal slot array," *IEEE Antennas Wireless Propag.* Lett., vol. 14, pp. 237–240, 2015.

[15] L. Chang, Y. Li, Z. Zhang, X. Li, S. Wang and Z. Feng, "Low-sidelobe air-filled slot array fabricated using silicon micromachining technology for millimeter-wave application," *IEEE Trans. Antennas Propag.,* vol. 65, no. 8, pp. 4067–4074, Aug. 2017.

[16] Y. J. Cheng, J. Wang and X. L. Liu, ":94 GHz substrate integrated waveguide dual-circular-polarization shared-aperture parallel-plate long-slot array antenna with low sidelobe level," *IEEE Trans. Antennas Propag.,* vol. 65, no. 11, pp. 5855–5861, Nov. 2017.

[17] H. Chu, P. Li and Y. X. Guo "A Beam-Shaping Feeding Network in Series Configuration for Antenna Array With Cosecant-Square Pattern and Low Sidelobes," *IEEE Antennas Wireless Propag. Lett.*, vol. 18, no. 4, pp. 742–746, Apr. 2019.

[18] R. Chopra and G. Kumar, "Series-fed binomial microstrip arrays for extremely low sidelobe level," *IEEE Trans. Antennas Propag.*, vol. 67, no. 6, pp. 4275–4279, Jun. 2019.

[19] J. Yin, Q. Wu, C. Yu, H. Wang and W. Hong, "Low-sidelobe-level series-fed microstrip antenna array of unequal interelement spacing," *IEEE Antennas Wireless Propag. Lett.*, vol. 16, pp. 1695–1698, 2017.

[20] S. Afoakwa and Y.-B. Jung, "Wideband microstrip comb-line linear array antenna using stubbed-element technique for high sidelobe suppression," *IEEE Trans. Antennas Propag.*, vol. 65, no. 10, pp. 5190–5199, Oct. 2017.

[21] R. Manikandan, P.K. Jawahar and P.H. Rao, "Low sidelobe level CSRR loaded weighted array antenna," *IEEE Trans. Antennas Propag.*, vol. 66, no. 12, pp. 6893–6905, Dec. 2018.

[22] D. Y. Kim and S. W. Nam, "Excitation control method for a low sidelobe SIW series slot array antenna with 45° linear polarization," *IEEE Trans. Antennas Propag.,* vol. 61, no. 11, pp. 5807–5812, Nov. 2013.

[23] Y. Geng, J. Wang, Y. Li, Z. Li, M. Chen and Z. Zhang, "High-efficiency leaky-wave antenna array with sidelobe suppression and multibeam generation," *IEEE Antennas Wireless Propag. Lett.*, vol. 16, pp. 2787–2790, 2017.

[24] Y. W. Wu, Z. Jiang and Z. C, Hao, "A 400-GHz low cost planar leaky-wave antenna with low sidelobe level and low cross-polarization level," *IEEE Trans. THz Sci. Technol.,* vol. 10, no. 4, pp. 427– 430, Jul. 2020.

[25] A. Wahid, M. Sreenivasan and P. H. Rao, "CSRR loaded microstrip array antenna with low side lobe level," *IEEE Antennas Wireless Propag. Lett.*, vol. 14, pp. 1169–1171, May 2015.

[26] D.-F. Guan, Z.-P. Qian, Y.-S. Zhang and Y. Cai, "Novel SIW cavity backed antenna array without using individual feeding network" *IEEE Antennas Wireless Propag. Lett.*, vol. 13, pp. 423–426, 2014.

[27] S. Ogurtsov and S. Koziel, "On alternative approaches to design of corporate feeds for low–sidelobe microstrip linear arrays," *IEEE Trans. Antennas Propag.*, vol. 66, no. 7, pp. 3781–3786, Jul. 2018.

[28] D. H. Nguyen, Ju. Ala-Laurinaho, J. Moll, V. Krozer, and G. Zimmer, "Improved sidelobe suppression microstrip patch antenna array by uniform feeding networks," *IEEE Trans. Antennas Propag.*, early access, DOI: 10.1109/TAP.2020.2995416.

[29] A. Vosoogh and P.-S. Kildal, "Simple formula for aperture efficiency reduction due to grating lobes in planar phased arrays", *IEEE Trans. Antennas Propag.*, vol. 64, no. 6, pp. 2263-2269, Jun. 2016.

[30] W. Lin and R. W. Ziolkowski, "High-directivity, compact, omnidirectional horizontally polarized antenna array," *IEEE Trans. Antennas Propag*., vol. 68, no. 8, pp. 6049–6058, Apr. 2020.

[31] C. A. Balanis, *Antenna Theory*, 3rd Ed. New York: John Wiley & Sons, 2005.

[32] R. W. Ziolkowski, "Using Huygens multipole arrays to realize unidirectional needle-like radiation," *Phys. Rev. X*, vol. 7, 031017, Jul. 2017.

[33] K.-M. Luk and H. Wong, "A new wideband unidirectional antenna element," *Int. J. Microw. Opt. Technol.*, vol. 1, no. 1, pp. 35–44, Jun. 2006.

[34] L. Ge and K.-M. Luk, "A low-profile magneto-electric dipole antenna," *IEEE Trans. Antennas Propag.*, vol. 60, no. 4, pp. 1684–1689, Apr. 2012.

[35] K.-M. Luk and B. Wu, "The magnetoelectric dipole—A wideband antenna for base stations in mobile communications," *Proc. IEEE*, vol. 100, no. 7, pp. 2297–2307, Jul. 2012.

[36] Y. Li and K.-M. Luk, "A multibeam end-fire magnetoelectric dipole antenna array for millimeter-wave applications," *IEEE Trans. Antennas Propag.*, vol. 64, no. 7, pp. 2894–2904, Jul. 2016.

[37] Y. Li, J. Wang, and K.-M. Luk, "Millimeter-wave multibeam aperture coupled magnetoelectric dipole array with planar substrate integrated beamforming network for 5G applications," *IEEE Trans. Antennas Propag.*, vol. 65, no. 12, pp. 6422–6431, Dec. 2017.

[38] N. Ashraf, A. R. Sebak, and A. A. Kishk, "Packaged microstrip line feed network on a single surface for dual-polarized 2N×2M ME-dipole antenna array," *IEEE Antennas Wireless Propag. Lett.*, vol. 19, no. 4, pp. 596-, Apr. 2020.

[39] R. W. Ziolkowski, "Low profile, broadside radiating, electrically small Huygens source antennas," *IEEE Access*, vol. 3, pp. 2644–2651, Dec. 2015.

[40] M. C. Tang, H. Wang and R. W. Ziolkowski, "Design and testing of simple, electrically small, low-profile, Huygens source antennas with broadside radiation performance," *IEEE Trans. Antennas Propag.*, vol. 64, no. 11, pp. 4607–4617, Nov. 2016.

[41] W. Lin and R. W. Ziolkowski, "Electrically-small, low-profile, Huygens circularly polarized antenna," *IEEE Trans. Antennas Propag*., vol. 66, no. 2, pp. 636–643, Feb. 2018.

[42] K. K. So, H. Wong, K. M. Luk and C. H. Chan, "Miniaturized circularly polarized patch antenna with low back radiation for GPS satellite communications," *IEEE Trans. Antennas Propag.,* vol. 63, no. 12, pp. 5934–5938, Dec. 2015.

[43] R. J. Mailloux, *Phased Array Antenna Handbook*, 2nd Ed. Norwood, MA: Artech House, 2005.

Wei LIN (Senior Member, IEEE) received the bachelor's and master's degrees in electronic engineering from the South China University of Technology, Guangzhou, China, in 2009 and 2012, respectively, and the Ph.D. degree in electronic engineering from the City University of Hong Kong, Hong Kong, in 2016.

He worked as a Research Associate with Nanyang Technological University, Singapore, from August 2012 to August 2013, and a Post-Doctoral Research Associate with the University of Technology Sydney, Ultimo, NSW, Australia, from October 2016 to September 2018, where he is currently a Chancellor's Post-Doctoral

Research Fellow with the Global Big Data Technologies Centre, School of Electrical and Data Engineering, Faculty of Engineering and IT. His research interests include the designs of circularly polarized antennas, electrically small antennas, reconfigurable antennas, HF antennas, satellite antennas, millimeter-wave antennas, wireless power transfer, terahertz devices, and their applications.

Dr. Lin has received many academic awards, which mainly include the Australia Research Council (ARC) Discovery Early Career Researcher Award (DECRA2021), the 2019 Raj Mittra Travel Grant (RMTG) from the IEEE AP-Society, the Best Paper Award (First Prize) at the International Symposium on Antennas and Propagation (ISAP 2018), the Best Young Professional Paper Award (First prize) at the 3rd Australian Microwave Symposium (AMS2018), the Best Poster Paper Award at the 2nd International Conference on Electromagnetic Materials and Technologies for the Future (EM-MTF2017), a Talent Development Scholarship from the Hong Kong Government, and the Young Scientist Award at the IEEE Region 10 Conference (TENCON2015). He was a recipient of an Outstanding Reviewer Award from the IEEE Antennas and Wireless Propagation Letters (2018) and the IEEE Transactions on Antennas and Propagation (2020).

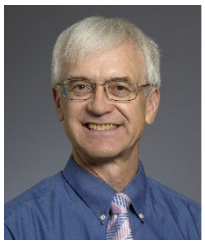

Richard W. Ziolkowski (Life Fellow, IEEE) received the B.Sc. (magna cum laude) degree (Hons.) in physics from Brown University, Providence, RI, USA, in 1974; the M.S. and Ph.D. degrees in physics from the University of Illinois at Urbana-Champaign, Urbana, IL, USA, in 1975 and 1980, respectively; and the Honorary Doctorate degree from the Technical University of Denmark, Kongens Lyngby, Denmark in 2012.

He is currently a Distinguished Professor in the Global Big Data Technologies Centre in the Faculty of Engineering and Information Technologies (FEIT) at the University of Technology Sydney, Ultimo NSW, Australia. He became a Professor Emeritus at the University of Arizona in 2018, where he was a Litton Industries John M. Leonis Distinguished Professor in the Department of Electrical and Computer Engineering in the College of Engineering and was also a Professor in the College of Optical Sciences. He was the Computational Electronics and Electromagnetics Thrust Area Leader with the Lawrence Livermore National Laboratory, Engineering Research Division, in Livermore, CA before joining The University of Arizona, Tucson, AZ, USA, in 1990.

Prof. Ziolkowski is the recipient of the 2019 IEEE Electromagnetics Award (IEEE Field Award). He is a Fellow of the Optical Society of America (OSA, 2006), and of the American Physical Society (APS, 2016). He was the Australian DSTO Fulbright Distinguished Chair in Advanced Science and Technology from 2014-2015. He was a 2014 Thomas-Reuters Highly Cited Researcher. He served as the President of the IEEE Antennas and Propagation Society in 2005. He is also actively involved with the URSI, OSA and SPIE professional societies.

His current research interests include the application of new mathematical and numerical methods to linear and nonlinear problems dealing with the interaction of electromagnetic and acoustic waves with complex linear and nonlinear media, as well as metamaterials, metamaterial-inspired structures, nano-structures, and other classical and quantum applications-specific configurations.